JPE

# Analysis and Design of a Multi-resonant Converter with a Wide Output Voltage Range for EV Charger Applications

Wenjin Sun*, Xiang Jin*, Li Zhang**, Haibing Hu†, and Yan Xing*

†*Jiangsu Key Laboratory of Renewable Energy Generation and Power Conversion, College of Automation Engineering, Nanjing University of Aeronautics and Astronautics, Nanjing, China
**Department of Electrical Engineering, Hohai University, Nanjing, China

**Abstract**

This paper illustrates the analysis and design of a multi-resonant converter applied to an electric vehicle (EV) charger. Thanks to the notch resonant characteristic, the multi-resonant converter achieve soft switching and operate with a narrowed switching frequency range even with a wide output voltage range. These advantages make it suitable for battery charging applications. With two more resonant elements, the design of the chosen converter is more complex than the conventional LLC resonant converter. However, there is not a distinct design outline for the multi-resonant converters in existing articles. According to the analysis in this paper, the normalized notch frequency $f_{r2n}$ and the second series resonant frequency $f_{r3n}$ are more sensitive to the notch capacitor ratio $q$ than the notch inductor ratio $k$. Then resonant capacitors should be well-designed before the other resonant elements. The peak gain of the converter depends mainly on the magnetizing inductor ratio $L_n$ and the normalized load $Q$. And it requires a smaller $L_n$ and $Q$ to provide a sufficient voltage gain $M_{max}$ at ($V_{o\_max}$, $P_{o\_max}$). However, the primary current increases with $(L_nQ)^{-1}$, and results in a low efficiency. Then a detailed design procedure for the multi-resonant converter has been provided. A 3.3kW prototype with an output voltage range of 50V to 500V dc and a peak efficiency of 97.3 % is built to verify the design and effectiveness of the converter.

**Key words:** DC-DC converter, multi-resonant converter, notch filter, battery charger

## I. INTRODUCTION

In the past decade, the challenges of reducing greenhouse gas emissions and finding a suitable means to provide clean energy are prompting the introduction of electric vehicles (EVs) and plug-in EVs (PEVs) [1-6]. Their large capacity battery stacks are normally charged from a public power line via an onboard charger (OBC). To realize fast charging, high-power chargers are relocated off-board in an external charging infrastructure to reduce cost, volume and weight. These chargers are referred as off-board chargers [3]. Instead of the bulky line frequency transformers, a modular design with a high frequency is widely adopted in off-board chargers to reduce the size and to improve the flexibility [3, 4]. For the OBC and the off-board charger modules, the two-stage structure is preferred. This structure includes: 1) an ac-dc converter for power factor correction (PFC) and harmonic reduction, and 2) a dc-dc converter for output control and galvanic isolation [1-6]. In isolated dc-dc converters, the size of the passive elements can be decreased by operating the converter with a high switching frequency. However, the frequency is limited by the switching loss. Then soft switching methods and resonant circuits are widely used to increase the switching frequency. Among the many candidates, one promising topology is the LLC resonant converter [6-9]. It can achieve ZVS turn-on of primary switches and soft commutation of secondary rectifiers over a wide load range. Since only a filter capacitor is needed, its output diodes' voltage stress is low. All these advantages make it suitable for charging applications [10, 11].

However, the LLC converter still has some issues to be

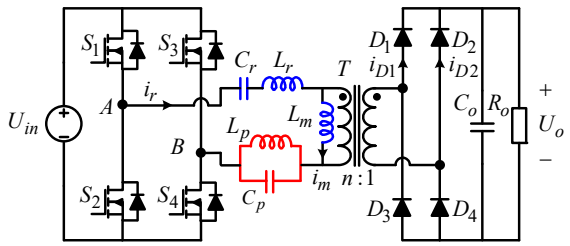


Fig. 1. Topology of a multi-resonant converter.

solved. Due to the flat voltage gain curves in the above resonant frequency region ($f_s > f_r$), the converter should be operated with a high frequency to provide a low output voltage, making the driver design difficult. Otherwise, the efficiency under normal operation is deteriorated with a small frequency range [12-16]. During start-up and short output conditions, the converter is also operated in the region ($f_s > f_r$) to avoid entering the ZCS zone [17]. Hence it is difficult to control the current and voltage stresses on the resonant tank, which may cause damage to semiconductor devices [18-20]. Some common solutions are introduced to solve these issues: pulse frequency modulation (PFM) control combined with pulse width control, PFM control combined with phase-shift control, and PFM control combined with burst mode control [13-16]. These solutions provide only qualitative analysis and may lose the primary switches' ZVS turn-on at low voltage and large current outputs. Based on the graphical state-trajectory analysis, optimal trajectory control strategies are proposed to solve the soft start-up and overload protection issues [18-20]. Owing to their complex calculations, they are difficult to implement for a wide output range.

Fortunately, these issues can be solved perfectly by introducing a notch filter into the existing LLC resonant tank [21-25]. In addition to achieving zero output within a small frequency range, the notch filter of the multi-resonant converter can also help the power delivery with third order harmonics injection [21, 22]. Since the location of the notch filter can be either at the primary side in Fig. 1 [21-24] or at the secondary side [25], there are two kinds of multi-resonant converters. In comparison with that one at the secondary side, the converter with a notch filter at the primary side is more suitable for vehicle charging applications with a high input voltage [25]. Its output gain characteristics are shown in Fig. 2. A topology with the same characteristics is provided in [26]. Although a third-order harmonics injection branch is more intuitive, the leakage inductance of the transformer cannot be directly merged into the resonant inductors during the parameter analysis and design. Then the analysis of the leakage inductance's impact on operation, and the converter's magnetic integration are more difficult than those in Fig. 1 [27, 28]. Based on the synthesis method of the resonant topologies in [28], another multi-resonant converter with the notch characteristic can be derived from an LCL resonant converter [28, 29]. However, without third-order harmonics

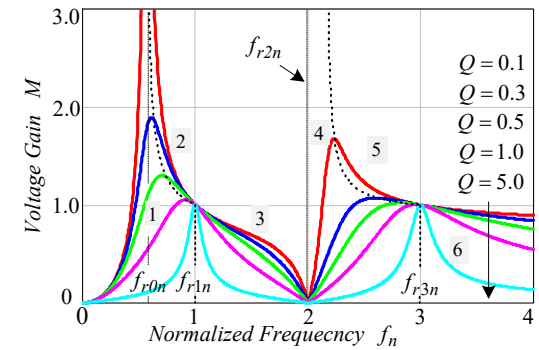


(a) Output voltage gain characteristics.

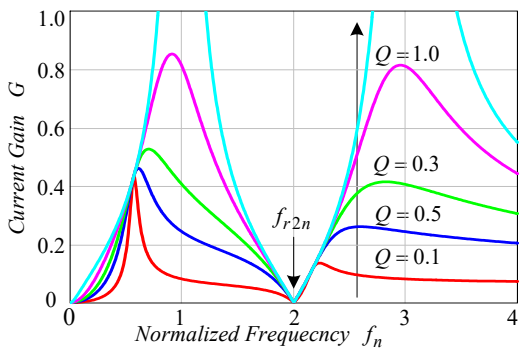


(b) Output current gain characteristics.

Fig. 2. Output gain characteristics of a multi-resonant converter: (a) output voltage gain; (b) output current gain.

injection, its high conduction loss results in a low efficiency.

With 2 more resonant elements, the analysis and design of the multi-resonant converter in Fig.1 are more complex than the conventional LLC converter. Based on the synthesis method in [28], the above merits of the chosen converter have been found intuitively, while the parameter effects are not obvious [21, 22]. To aid in understanding, the converter has also been analyzed with the impedance of the series resonant tank and the parallel tank in [23, 24]. However, the analysis is too complicated, and the effects of the inductor ratio $k$ and the capacitor ratio $q$ on the converter are still unclear. Due to its complexity, the resonant parameters of the multi-resonant converter in [21-24] are simply designed during the operation region $f_s \le f_{r1}$ by using the design method of the conventional *LLC* resonant converter. However, these designs do not cover the operation region $f_{r1} < f_s \le f_{r2}$, which is also utilized for a wide output range, as in EV chargers. The following sections will focus on the parameter analysis and design of a multi-resonant converter with a wide output range.

## II. Operational Principles

The topology of a multi-resonant converter with a primary notch filter is shown in Fig. 1. The PFM control is adopted to control the output. And Fig. 3 shows typical waveforms of the converter below the resonant frequency $f_{r1}$. Due to

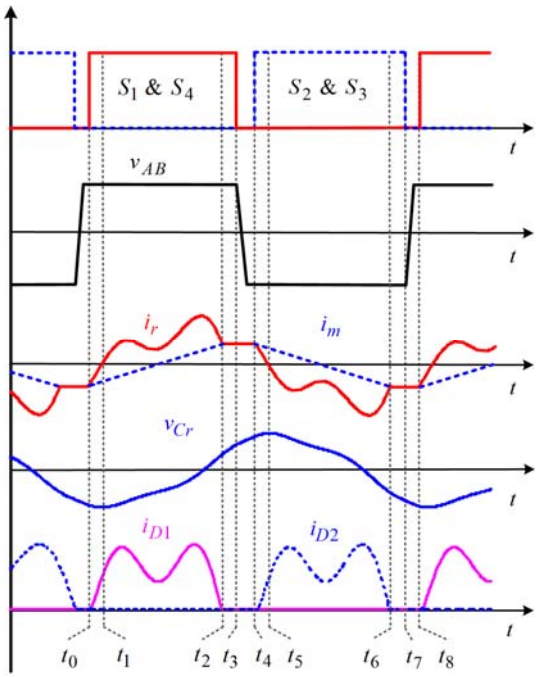


Fig. 3. Typical waveforms of a multi-resonant converter below the resonant frequency $f_{r1}$.

limitations on space and its simplicity, the mode analysis is not provided here. Based on the FHA analysis [17], the converter in Fig. 1 can be simplified to the linear circuit in Fig. 4 with an equivalent load resistor.

$$R_e = \frac{8n^2 R_o}{\pi^2} \tag{1}$$

Where, $n$ is the turn ratio of the transformer.

Then four important resonant frequencies can be obtained from Fig. 4: the parallel resonant frequency $f_{r0}$ to step up the output voltage, the notch resonant frequency $f_{r2}$ to step down the output voltage to as low as zero, and the two series resonant frequency $f_{r1}$ and $f_{r3}$ to transfer energy at a high efficiency.

$$f_{r0} = \frac{1}{\sqrt{(1+k+\frac{1}{L_n})q}} f_r \tag{2}$$

$$f_{r1} = \sqrt{\frac{1+kq+k-\sqrt{(1+kq+k)^2-4kq}}{2kq}} f_r \tag{3}$$

$$f_{r2} = \frac{1}{2\pi}\frac{1}{\sqrt{L_p C_p}} = \frac{1}{\sqrt{kq}} f_r \tag{4}$$

$$f_{r3} = \sqrt{\frac{1+kq+k+\sqrt{(1+kq+k)^2-4kq}}{2kq}} f_r \tag{5}$$

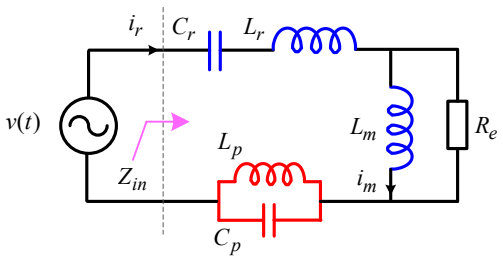


Fig. 4. Simplified circuit of a multi-resonant converter.

Where:

$$\begin{cases} L_n = \frac{L_m}{L_r}, k = \frac{L_p}{L_r}, q = \frac{C_p}{C_r}, \\ f_r = \frac{1}{2\pi\sqrt{L_r C_r}}, Z_r = \sqrt{\frac{L_r}{C_r}}, Q = \frac{Z_r}{R_e}. \end{cases} \tag{6}$$

From Fig. 4, the normalized output voltage gain $M$ of the multi-resonant converter can be derived and given as Eq. (7) at the bottom of this page, where the switching frequency $f_s$ is normalized as:

$$\begin{cases} f_n = \frac{f_s}{f_{r1}}, \\ g = \frac{f_{r1}}{f_r} = \sqrt{\frac{1+kq+k-\sqrt{(1+kq+k)^2-4kq}}{2kq}}. \end{cases} \tag{8}$$

In addition, the normalized current gain $G$ can be obtained as:

$$G = \frac{I_o / n}{U_{in} / Z_r} = \frac{8Q}{\pi^2} M. \tag{9}$$

Fig. 2 shows the output voltage and current gain characteristics of the converter. The four resonant frequencies are also marked in Fig. 2 (a). Functioning in the role of a conventional LLC converter, the resonant frequency $f_{r1}$ helps to deliver the fundamental component to the load, while the frequency $f_{r0}$ helps boost the output [17, 28]. Moreover, the additional resonant frequency $f_{r3}$ of the multi-resonant converter can provide very low impedance for higher order harmonics. Consequently, the injection of higher order harmonics can enhance the power delivery to reduce the reactive power and conduction losses [21-25]. Due to the notch frequency $f_{r2}$, the voltage gain $M$ and current gain $G$ of the multi-resonant converter can achieve zero in a much smaller frequency range than the conventional LLC converter, making it beneficial during the start-up and short output circuit conditions.

In Fig. 4, the normalized input impedance $Z_{inN}$ of the multi-resonant converter can be calculated as Eq. (10). Like the conventional LLC converter, it should be inductive to achieve ZVS turn-on of the primary switches. With the imaginary part of $Z_{inN}$ zero, the boundary $Q_B$ between the capacitive and

$$M(k,q,L_n,Q,f_n) = \frac{nV_o}{V_{in}} = \frac{1}{\sqrt{[1+\frac{1}{L_n}(1-\frac{1}{g^2 f_n^2}-\frac{k}{kqg^2 f_n^2-1})]^2 + [gf_n Q(1-\frac{1}{g^2 f_n^2}-\frac{k}{kqg^2 f_n^2-1})]^2}} \tag{7}$$

$$Z_{inN}(k,q,L_n,Q,f_n) = \frac{Z_{in}}{Z_r} = \frac{Q}{Q^2 + L_n^2 (gf_n)^{-2}} + j[gf_n(1-\frac{1}{g^2 f_n^2}-\frac{k}{kqg^2 f_n^2-1}) + \frac{L_n (gf_n)^{-1}}{Q^2 + L_n^2 (gf_n)^{-2}}] \tag{10}$$

inductive region can be derived as Eq. (11). And the voltage gain $M_B$ at the boundary, the dashed line in Fig. 2(a), can be obtained as Eq. (12). With the boundaries and the notch frequency $f_{r2}$, the curves in Fig. 2(a) can be divided into 6 operation regions: Region 1 ($f_n<f_{r1n}$ and on the left of the boundary), Region 2 ($f_{r0n}<f_n<f_{r1n}$ and on the right of the boundary), Region 3 ($f_{r1n}<f_n<f_{r2n}$), Region 4 ($f_{r2n}<f_n<f_{r3n}$ and on the left of the boundary), Region 5 ($f_{r2n}<f_n<f_{r3n}$ and on the right of the boundary), and Region 6 ($f_n>f_{r3n}$). The input impedance is inductive in Region 2, 3, 5 and 6, while it is capacitive in Region 1 and 4. In order to provide soft start-up and short output protection within a small frequency range, it is preferred to operate the converter in Region 2 and 3, which are below the notch frequency $f_{r2}$.

$$Q_B(k,q,L_n,f_n)=\frac{L_n}{gf_n}\sqrt{\frac{1}{L_n(\frac{1}{g^2f_n^2}+\frac{k}{kqg^2f_n^2-1})}-1} \quad (11)$$

$$M_B(k,q,L_n,f_n)=\frac{1}{\sqrt{1+L_n(1-\frac{1}{g^2f_n^2}-\frac{k}{kqg^2f_n^2-1})}} \quad (12)$$

## III. Analysis of the Circuit Parameters

Despite the magnetizing inductor ratio $L_n$ and the normalized load $Q$, the output voltage gain $M$ in Eq. (7) also depends on the ratio $k$ and $q$. With so many parameters, the design of the converter becomes more complex. Before the design, the effects of these parameters should be addressed. Since the charger requires a wide output voltage and a high efficiency, the following analysis will focus on the voltage gain $M$ and the primary current.

### *A. The Effects of k and q on the Voltage Gain M*

With Eq. (7), output voltage gain curves with different values for $k$ and $q$ are plotted in Fig. 5 (a) and (b). It can be seen that the ratio $k$ and $q$ only decide the notch point $f_{r2n}=f_{r2}/f_{r1}$ and the second series resonant point $f_{r3n}=f_{r3}/f_{r1}$, while they have little effect on the peak gain of the curves. Fig.5 (c) shows variations of the frequencies $f_{r2n}$ and $f_{r3n}$ with respect to $k$ or $q$ at $k=15/16$ and $q=0.6$. In Fig. 5 (b) and (c), the values of $f_{r2n}$ and $f_{r3n}$ decrease with an increase of $q$. Unlike $q$, the value of $f_{r3n}$ in Fig. 5 (c) is at its minimum with an increase of $k$, while the value of $f_{r2n}$ approaches its lower limit. In terms of the two black marks shown in Fig. 5 (c), $f_{r3n}$ is more sensitive to the variable $q$ than the variable $k$ *at* $k=15/16$ and $q=0.6$. In addition, $q$ has a wider regulation of $f_{r2n}$ than $k$ when $f_{r2n}<2$. Then the resonant capacitors $C_p$ and $C_r$ should be well-designed before the other resonant elements.

### *B. The Effects of k and q on the primary current*

In order to make full use of the third order harmonic of the primary voltage $v_{AB}$ to help the energy transfer, $f_{r3n}$ is located at 3 [21-26]. Then the notch point $f_{r2n}$ is the only one decided

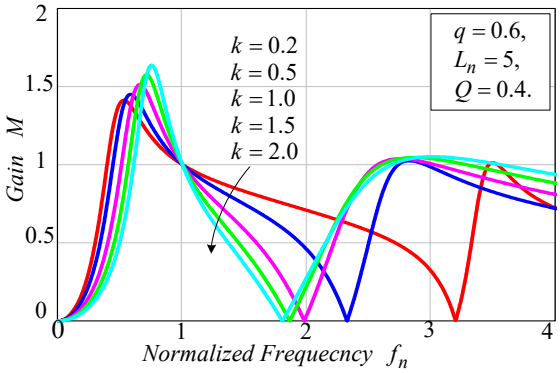


(a) DC gain curves with different values of $k$.

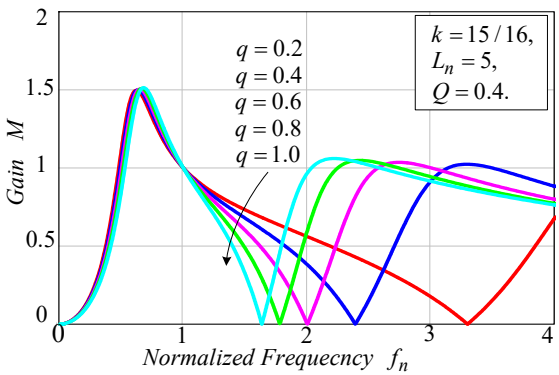


(b) DC gain curves with different values of $q$.

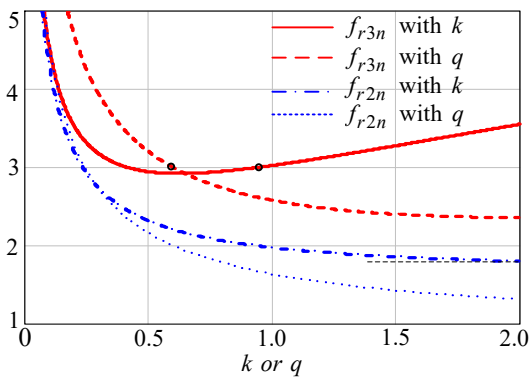


(c) Normalized frequencies $f_{r2n}$ and $f_{r3n}$ with $k$ or $q$.

Fig. 5. (a) DC gain curves with different values of $k$ at $q$=0.6, $L_n$=5, and $Q$=0.4; (b) DC gain curves with different values of $q$ at $k$=15/16, $L_n$=5, and $Q$=0.4; (c) Variations of the normalized frequencies $f_{r2n}$ and $f_{r3n}$ with $k$ or $q$ at $k$ =15/16, q=0.6.

by $k$ and $q$. From the simulations at $f_s=f_{r1}$, Fig. 6 gives the normalized primary RMS current $I_{Lr}/(I_o/n)$ with different values of $f_{r2n}$. As $f_{r2n}$ is designed close to $f_{r1n}$=1 or $f_{r3n}$=3, the primary current $I_{Lr}/(I_o/n)$ become larger, since more energy is trapped by the notch filter section [21]. Since the primary current is lowest at $f_{r2n}$=2, it is appropriate to locate the notch point $f_{r2n}$ around 1.5~2.5 to decrease the conduction loss.

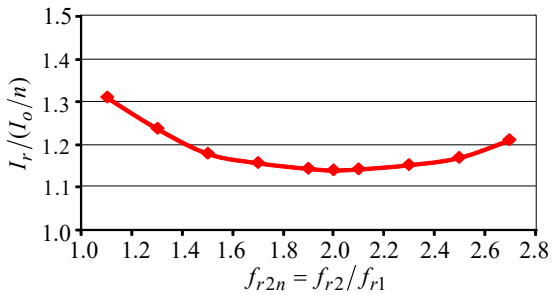


Fig. 6. Normalized primary current at $f_s$=$f_{r1}$ with different notch resonant frequencies $f_{r2}/f_{r1}$.

### C. *The Effects of $L_n$ and $Q$ on the Voltage Gain $M$*

With constant $k$ and $q$, the output voltage gain curves with different $Q$ and $L_n$ are shown in Fig. 2 (a) and Fig. 7. Unlike $k$ and $q$, $Q$ and $L_n$ have a strong impact on the peak gain of the curves, while they have no impact on the resonant points $f_{r2n}$ and $f_{r3n}$. The peak gain at $f_n$≤1 decreases with increases of $L_n$ and $Q$. Then they should not be too large to provide the voltage gain required by the charger specifications.

### D. *The Effects of $L_n$ and $Q$ on the primary current*

To simplify the analysis, the normal operation point at $f_s$=$f_{r1}$, namely $t_3$-$t_2$=0 in Fig. 3, is used to analyze the primary current and magnetizing current. Since $L_m$ is too large and the impedance composed of $L_r$, $C_r$, $L_p$ and $C_p$ is zero at $f_n$=1 and $f_n$=3, the input impedance $Z_{in}$ at the fundamental and third order harmonics can be assumed to be the same. Then the primary current $i_r$ can be expressed as:

$$i_r(t) = I_p \sin(\omega_{r1}(t-t_0)+\varphi) + \frac{I_p}{3}\sin(3\omega_{r1}(t-t_0)+\varphi). \quad (13)$$

Where, $I_p$ is the peak current of the fundamental harmonic, $w_{r1}$ is the angular frequency $2\pi f_{r1}$, and $\varphi$ is the phase difference between the voltage $v_{AB}$ and the fundamental harmonic of the resonant current $i_r$.

Since the voltage across the magnetizing inductor $L_m$ is clamped by the reflected output voltage $nU_o$, its current can be expressed as:

$$i_m(t) = \begin{cases} I_m[4(t-t_0)f_{r1}-1] & t_0 \le t < t_0 + \dfrac{1}{2f_{r1}} \\ I_m[3-4(t-t_1)f_{r1}] & t_0 + \dfrac{1}{2f_{r1}} \le t < t_0 + \dfrac{1}{f_{r1}} \end{cases} \quad (14)$$

Where, $t_0$ is the initial time in Fig. 3, and $I_m$ is the peak current of $L_m$ that can be calculated as:

$$I_m = \frac{nV_o}{4L_m f_{r1}}. \quad (15)$$

Since $i_{Lr}$ is equal to $i_{Lm}$ at $t_1$:

$$i_r(t_0) = \frac{4}{3} I_p \sin\varphi = -I_m. \quad (16)$$

The load current of the converter can be obtained by averaging the input current of the bridge rectifiers $D_1$ - $D_4$ during a half cycle.

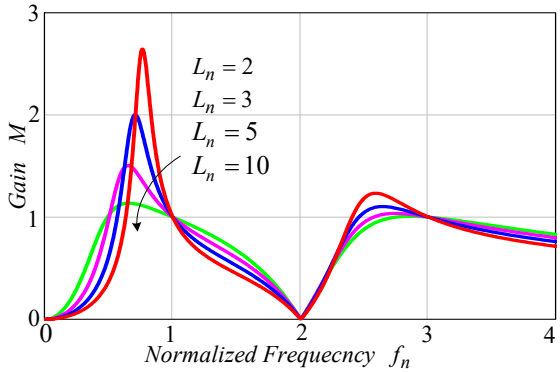


Fig. 7. DC gain curves with different values of $L_n$.

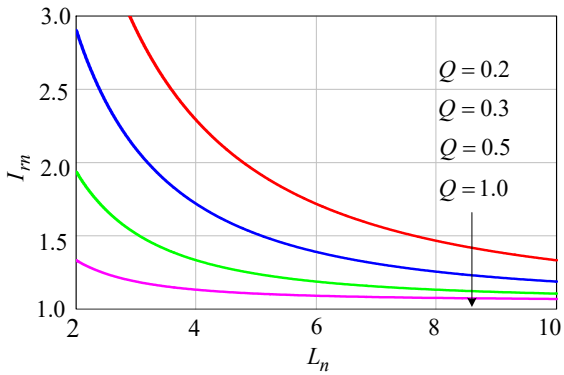


Fig. 8. Normalized primary RMS current $I_{rn}$ with different values of $L_n$ and $Q$.

$$I_o = 2nf_{r1}\int_{t0}^{t0+\frac{1}{2f_{r1}}} [i_r(t) - i_m(t)]dt \quad (17)$$

Combing Eq. (1), (6), (8), and (13) - (17), the normalized peak current $I_{mn}$ and $I_{pn}$ can be obtained as:

$$I_{mn} = \frac{I_m}{I_o/n} = \frac{\pi^3}{16gL_nQ} \quad (18)$$

$$I_{pn} = \frac{I_p}{I_o/n} = \frac{3\pi}{4}\sqrt{\frac{\pi^4}{256g^2(L_nQ)^2} + \frac{9}{25}}. \quad (19)$$

The normalized RMS currents $I_{rn}$ and $I_{Secn}$ of the transformer's primary and secondary side can be obtained as Eq. (20) and (21). As shown in Fig. 8, the value of $I_{rn}$ decreases with $L_n^{-1}$, $Q^{-1}$, and $(L_nQ)^{-1}$. In addition, $I_{Secn}$ and $I_{mn}$ have the same trends. In order to increase efficiency, $L_nQ$ should be large enough to reduce the conduction loss and switching loss.

$$I_{rn} = \sqrt{(\frac{I_{pn}}{\sqrt{2}})^2 + (\frac{I_{pn}}{3\sqrt{2}})^2} = \frac{\pi}{4}\sqrt{\frac{\pi^4}{51.2g^2(L_nQ)^2} + \frac{9}{5}} \quad (20)$$

$$I_{Secn} = \frac{1}{I_o/n}\sqrt{2n^2 f_{r1}\int_{t0}^{t0+\frac{1}{2f_{r1}}} [i_r(t) - i_m(t)]^2 dt} = n\pi\sqrt{\frac{93\pi^4 - 896\pi^2}{36864g^2(L_nQ)^2} + \frac{9}{80}} \quad (21)$$

TABLE I.

DESIGN SPECIFICATIONS AND PARAMETERS.

| | Parameters | Value |
|---|---|---|
| Design Spec. | Input : $V_{in\_nom}$ ($V_{in\_min}$~$V_{in\_max}$) | 400V ±10 V |
| | Output : $V_{o\_nom}$ ($V_{o\_min}$~$V_{o\_max}$) | 400V(50~500V) |
| | Output Power at 400V : $P_{o\_nom}$ | 3300 W |
| | Output Current at 400V : $I_{o\_nom}$ | 8.25 A |
| | Resonant Frequency : $f_{r1}$ | 100 kHz |
| Design Parameters | Max. frequency $f_s$ at 300V: $f_{max}$ | 140 kHz |
| | Transformer Ratio : $n$ | 24:24 |
| | Ratio of $L_m$ to $L_r$ : $L_n$ | 5 |
| | Resonant Inductor : $L_r$, $L_p$ | 40 μH, 37.5μH |
| | Resonant Capacitor : $C_r$, $C_p$ | 28.5 nF, 16.8nF |
| | Magnetizing Inductance : $L_m$ | 200 μH |
| | Dead Time : $t_{dead}$ | 200 ns |

## IV. DESIGN PROCEDURE

From the above analysis, it is preferred to operate the converter in Region 2 and Region 3. Compared with the fundamental harmonic, the energy transferred through the third order harmonic is less [21-26]. With $f_{r2n}$ and $f_{r3n}$ fixed, the design of the converter focuses solely on Region 2 and Region 3 below $f_{r2n}$, as shown in Fig. 9. The following is the step-by-step design procedure. For illustration, a charger with the design criteria in Table I is designed.

### A. Calculating the Ratios k and q

Substituting $f_{r2n}$ and $f_{r3n}$ into Eq. (3) - (5) and Eq. (8), the values $k$ and $q$ can be calculated as Eq. (22). Since $f_{r3n} > f_{r2n}$ and $f_{r2n} > 1$, both $k$ and $q$ have positive values. From the above analysis, it is better to locate $f_{r2n}$ and $f_{r3n}$ at 2 and 3 to reduce the conduction loss. Then $k$=*15/16*, $q$=*0.6*, and g=2/3 can be obtained.

$$\begin{cases} k = \dfrac{(f_{r3n}^2 - f_{r2n}^2)(f_{r2n}^2 - 1)}{f_{r2n}^4}, \\ q = \dfrac{f_{r3n}^2}{(f_{r3n}^2 - f_{r2n}^2)(f_{r2n}^2 - 1)}, \\ g = \dfrac{f_{r2n}}{f_{r3n}}. \end{cases} \tag{22}$$

### B. Selecting the Transformer Turns Ratio n

Like the conventional LLC converter, the turn ratio of the transformer should be selected at the unity gain, namely at $f_s$= $f_{r1}$. Then it can be calculated as:

$$n = \frac{V_{in\_norm}}{V_{o\_norm} + 2V_F} \tag{23}$$

Where, $V_F$ is the diode voltage drop of the output rectifier.

### C. Selecting the Ratio $L_n$

For a vehicle charger, the output power is low at an output voltage below $V_{o\_m}$. Then it is beneficial to keep a high efficiency at an output above $V_{o\_m}$. It is chosen as 300V here. Substituting $Q$=0 into Eq. (7), the zero-load gain of the converter can be obtained as:

$$M_o = \frac{1}{1 + L_n\left(1 - \dfrac{1}{g^2 f_n^2} - \dfrac{k}{kqg^2 f_n^2 - 1}\right)}. \tag{24}$$

Since $k$ and $q$ are fixed, the ratio $L_n$ in Eq. (24) cannot be too large. Otherwise, the switching frequency exceeds the maximum switching frequency $f_{nmax}$ at the minimum voltage gain $M_{min}$ in Fig. 9. As shown in Fig. 10, $L_n$ should be in the shadow below the boundary to achieve $M_{min}$ at $V_{o\_m}$, and its maximum value can be calculated as follows:

$$L_n = \left(\frac{1}{M_o} - 1\right)\frac{f_{n\max}^2 (f_{r2n}^2 - f_{n\max}^2)}{(f_{n\max}^2 - 1)(f_{r3n}^2 - f_{n\max}^2)}. \tag{25}$$

With an increase of $f_{nmax}$, a larger $L_n$ can be obtained to reduce the conduction loss and to increase the efficiency. However, as shown in Fig. 9, the gain slope is steeper as $f_n$ approaches $f_{r2n}$, making it too sensitive to control. After the trade-off, $f_{nmax}$ and $L_n$ are chosen as 1.4 and 5 here.

### D. Normalized Load $Q_{max}$

Providing a sufficient voltage gain $M_{max}$ at ($V_{o\_max}$, $P_{o\_max}$), the maximum normalized load $Q_{max}$ should be as large as possible to reduce the conduction loss. Then the operation point can be placed at the boundary in Fig. 9. Substituting

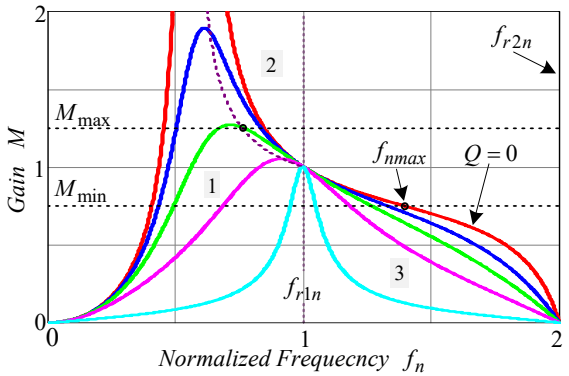


Fig. 9. DC gain curves for design considerations.

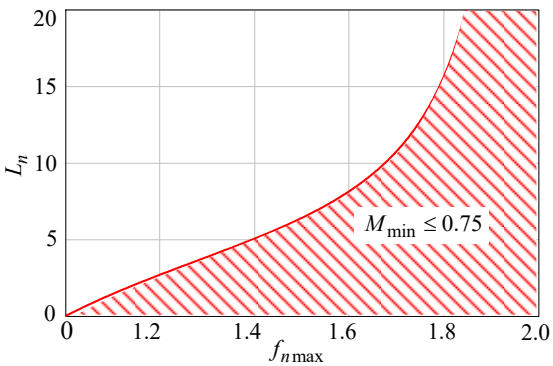


Fig. 10. Choice of $L_n$ to provide the minimum voltage gain $M_{min}$ with different values of $f_{nmax}$.

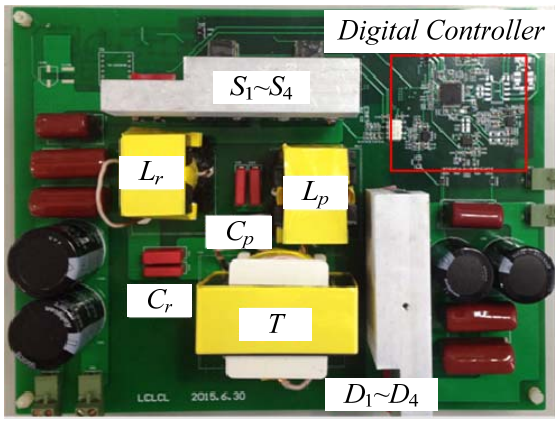


Fig. 11. Experimental prototype.

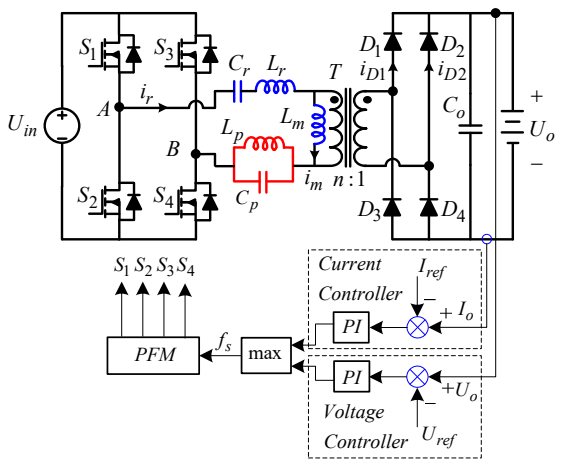


Fig. 12. Control block of the charger.

$M$=$M_{max}$ into Eq. (12), $f_{nmin}$ can be derived as Eq. (26), and 0<$f_{nmin}$<1. With $f_n$=$f_{nmin}$, $Q_{max}$ can be obtained as follows from Eq. (11).

$$Q_{\max}=\frac{L_n}{gf_{n\min}\sqrt{M_{\max}^2-1}} \tag{27}$$

### *E. Calculating the Resonant Parameters*

With the equivalent load resistor $R_e$ at ($V_{o\_max}$, $P_{o\_max}$), the value of the resonant capacitors $C_r$ are given by Eq. (28). Then $C_p$ can be obtained with Eq. (6) and (22).

$$C_r=\frac{g}{2\pi f_{r1}Q_{max}R_e} \tag{28}$$

If $C_r$ and $C_p$ are not appropriate values for commercial product selection, they can have fine tuning during the above steps. Once the resonant capacitors are determined, the resonant inductors $L_r$, $L_p$ and transformer's magnetizing inductor $L_m$ can be calculated using Eq. (29), (6) and (25).

TABLE II.

KEY COMPONENT USED IN THE PROTOTYPE.

| *Component* | *Part #* |
|---|---|
| Switches: $S_1$~$S_4$ | SPW35N60C3 |
| Rectifiers: $D_1$~$D_4$ | BYR29 |
| Resonant Capacitor: $C_r$ | MKP10-28.5 nF |
| Resonant Capacitor: $C_p$ | MKP10-16.8 nF |
| Resonant Inductor: $L_r$ | PQ35/35- PC40 |
| Resonant Inductor: $L_p$ | PQ40/40- PC40 |
| Transformer: $T$ | EE65/32/27-PC40 |

TABLE III.

PARAMETERS OF THE CONVERTERS FOR COMPARISON.

| | *Parameters* | *MRC* **I** | *MRC* **II** | *LLC* |
|---|---|---|---|---|
| **Design Parameters** | $f_{r1}$ | 100 kHz | 100kHz | 100kHz |
| | $f_{max}$ at 300V | 140 kHz | 120kHz | 140kHz |
| | $f_s$ at 300~500V | 80~140 kHz | 90~120kHz | 80~140kHz |
| | *Ratio n* | 24:24 | 24:24 | 24:24 |
| | *Ratio* $L_n$ | 5 | 2.5 | 2 |
| | *Inductor* $L_r$ | 40 μH | 57uH | 80uH |
| | *Inductor* $L_p$ | 37.5μH | 53uH | - |
| | *Capacitor* $C_r$ | 28.5 nF | 20 nF | 33nF |
| | *Capacitor* $C_p$ | 16.8nF | 12nF | - |
| | *Inductance* $L_m$ | 200 μH | 140uH | 160uH |

$$L_r=\frac{g^2}{4\pi^2 f_{r1}^2 C_r} \tag{29}$$

## V. EXPERIMENTAL RESULTS

A prototype of the full-bridge multi-resonant converter shown in Fig. 11 was built to provide experimental evaluations. Table II gives the key components used in the prototype converter. The control block of the charger is provided in Fig. 12, and it contains two separate controllers for the constant current control and constant voltage control. The switching frequency $f_s$ is in the range of $f_{min}$ to $f_{r2}$.

Fig. 13 shows calculated loss comparisons between the multi-resonant converter (MRC) and the conventional LLC converter at a 400V/3300W output. Two multi resonant converters with different $L_n$ have been designed. And the resonant tank parameters of the three converters are provided in the Table III. Since they have the same output current, the diode conduction losses of the three converters are equal to each other in Fig. 13. It can also be found that a

$$f_{nmin}=\frac{1}{g}\sqrt{\frac{kq+k+[1-\frac{1}{L_n}(\frac{1}{M_{max}^2}-1)]-\sqrt{[kq+k+(1-\frac{1}{L_n}(\frac{1}{M_{max}^2}-1))]^2-4kq[1-\frac{1}{L_n}(\frac{1}{M_{max}^2}-1)]}}{2kq[1-\frac{1}{L_n}(\frac{1}{M_{max}^2}-1)]}} \tag{26}$$

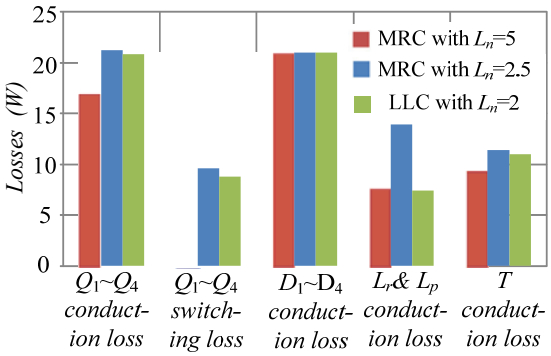


Fig. 13. Calculated losses comparison between the multi-resonant converter (MRC) and the conventional LLC converter at a 400V/3300W output.

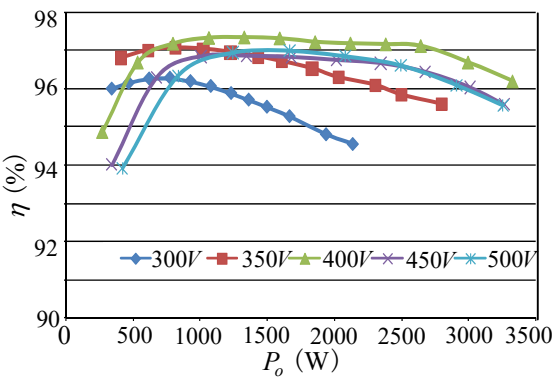


Fig. 14. Measured Efficiency at $V_{in}$= 400V.

multi-resonant converter with a higher $f_{max}$ can have a larger magnetizing inductor ratio $L_n$, and it reduces a lot of the conduction losses, which has been verified by the above theoretical analysis. With the same switching frequency range at a 300V-500V output, the multi resonant converter with $L_n$=5 can also cut down the conduction losses from the widely used LLC converter, owing to the reduction of the primary RMS current with the injection of third-order harmonics. Efficiency curves of the converter with $L_n$=5 are given in Fig. 14 for output voltages of 300V, 350V, 400V, 450V and 500V. And a peak efficiency of 97.3% has been achieved.

Fig. 15 shows experimental waveforms of the $S_1$ driver voltage ($v_{GS1}$), resonant tank current ($i_r$), and output voltage ($v_o$) at the start-up and short output protection. Thanks to the notch characteristic of the resonant tank, the resonant current $i_r$ does not have a large surge current during either the start-up procedure or short output protection as is the case with the conventional LLC converter, which increases reliability of the MOSFETs. Although the switching frequency of the converter is just $f_{r2}$=200 kHz at the short output, the converter can still be in steady operation with a small resonant current.

Fig. 16 shows experimental waveforms under normal

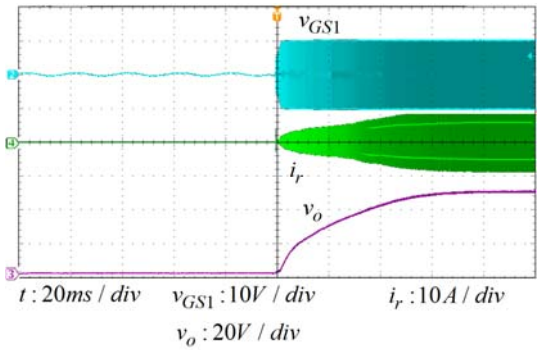


(a) Waveforms during the start-up condition.

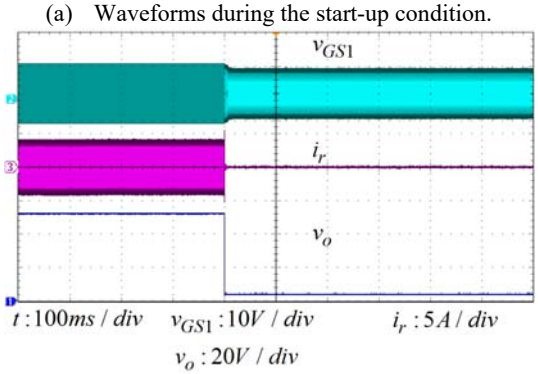


(b) Waveforms during the short output protection.

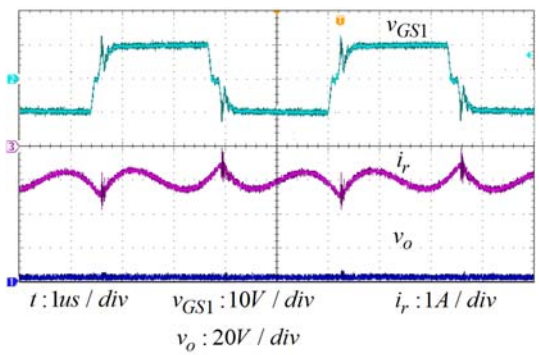


(c) Stable waveform during the short output condition.

Fig. 15. Waveforms of the $S_1$ driver voltage ($v_{GS1}$), resonant tank current ($i_r$), and output voltage ($v_o$): (a) during the startup condition; (b) during short output protection; (c) stable waveform during the short output condition.

operation at $V_{in}$ = 400 V. With third order harmonics injection, the current waveforms $i_r$ are saddle-shaped, as shown in Fig. 16 (a). It is very close to a square waveform with a low RMS current under nominal operation, which results in low conduction losses. Fig. 16 (b) presents waveforms at the maximum output voltage and power 500 V/3300 W with a minimum frequency of 81 kHz. In addition, Fig. 16(c) provides waveforms at a 300 V/300 W output with a frequency of 128 kHz. In Fig. 16 (b) and (c), the two design points, both in critical situations, have achieved ZVS turn-on. And it has verified the effectiveness of the proposed design method. Moreover, it can be seen from Fig. 16 (d) that the

primary switches can achieve ZVS turn-on at the minimum output voltage 50 V, while this is difficult for the conventional LLC converter.

## VI. CONCLUSIONS

A multi-resonant converter with a notch filter has been chosen for vehicle charging applications. It has been found that the notch capacitor ratio $q$ has a stronger impact on the normalized notch frequency $f_{r2n}$ and the second series resonant frequency $f_{r3n}$ than the notch inductor ratio $k$. Therefore, the resonant capacitors $C_p$ and $C_r$ should be well-designed before the other resonant elements. Unlike $k$ and $q$, the magnetizing inductor ratio $L_n$ and the normalized load $Q$ determine the peak gain of the curves. By providing a sufficient voltage gain $M_{max}$ at ($V_{o\_max}$, $P_{o\_max}$), the primary current decreases with $(L_nQ)^{-1}$, which depends on the maximum switching frequency $f_{nmax}$ under normal operation. Based on the above analysis, a detailed design procedure for the multi- resonant converter has been provided.

Experimental results show that the chosen converter can achieve a wide output range 50V-500V within a small frequency range, soft start-up and short output protection without a large surge current in the resonant tank. Furthermore, the converter can achieve stable operation with a small current at the short output. In spite of two additional resonant elements, the chosen converter can still gain a high efficiency due to the injection of third order harmonics. With these advantages over the LLC converter, the multi-resonant converter with a primary notch filter is more promising for the vehicle charging applications.

## ACKNOWLEDGMENT

This work was supported in part by the National Key R&D Program of China under Grant 2016YFB0601603, and in part by the National Natural Science Foundation of China under Grant 51677054.

## REFERENCES

[1] A. Y. Saber and G. K. Venayagamoorthy, "Plug-in vehicles and renewable energy sources for cost and emission reductions," *IEEE Trans. Ind. Electron.*, vol. 58, no. 4, pp. 1229–1238, Apr. 2011.

[2] Yihua Hu, Rong Zeng, Wenping Cao, Jiangfeng Zhang, et al, "Design of a High-power, High Step-up Ratio Modular DC-DC Converter by the Matrix Transformer Approach," *IEEE Trans. Ind. Electron.*, Vol. 63, No. 4, pp. 2190-2202, Apr. 2016.

[3] A. Khaligh and S. Dusmez, "Comprehensive Topological Analysis of Conductive and Inductive Charging Solutions for Plug-In Electric Vehicles," *IEEE Trans. Veh. Technol.*, Vol. 61, No. 8, pp.3475-3489, Oct. 2012.

[4] M. Yilmaz and P. T. Krein, "Review of charging power

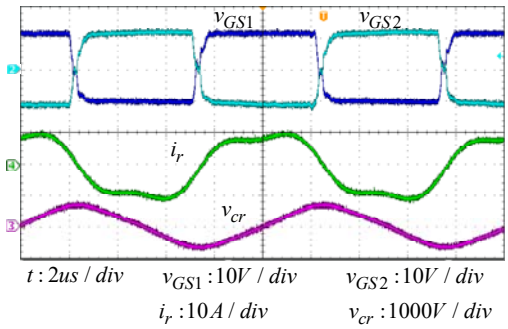


(a) $Vo$ = 400 V, $Po$ = 3300 W.

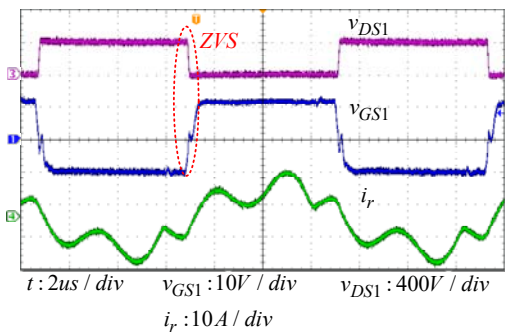


(b) $Vo$ = 500 V, $Po$ = 3300 W.

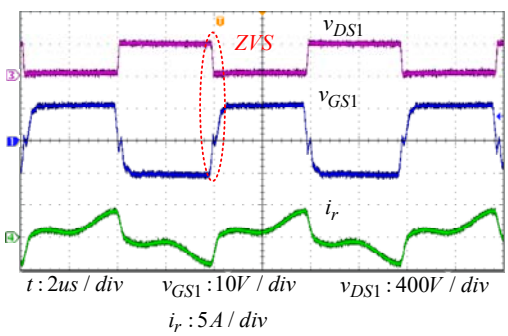


(c) $Vo$ = 300 V, $Po$ = 300 W.

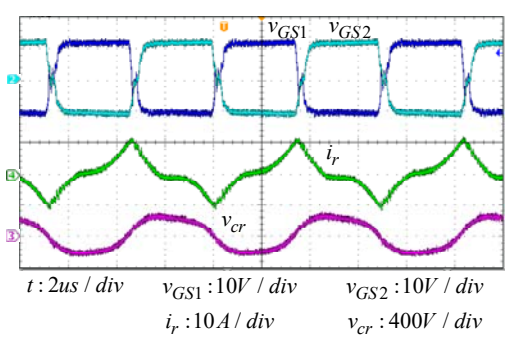


(d) $Vo$ = 50 V, $Po$ = 200 W.

Fig. 16. Waveforms of the $S_1$ driver voltage ($v_{GS1}$), voltage across $S_1$ ($v_{DS1}$), and resonant tank current ($i_r$) at different loads: (a) $Vo$ = 400 V, $Po$ = 3300 W; (b) $Vo$ = 500 V, $Po$ = 3300 W; (c) $Vo$ = 300 V, $Po$ = 300 W; (c) $Vo$ = 50 V, $Po$ = 200 W.

levels and infrastructure for plug-in electric and hybrid vehicles," in *Proc. IEEE Elect.Veh. Conf.*, pp. 1–8, 2012.
[5] Y. Jang, M. M. Jovanović, J. M. Ruiz, M. Kumar, and G. Liu, "Implementation of 3.3-kW GaN-Based DC-DC Converter for EV On-Board Charger with Series-Resonant Converter that Employs Combination of Variable-Frequency and Delay-Time Control," in *Proc. IEEE Appl. Power Electron. Conf. Expo.*, pp. 1292-1299, 2016.
[6] F. Musavi, M. Craciun, D.S. Gautam, W. Eberle, W.G. Dunford, "An LLC Resonant DC-DC Converter for Wide Output Voltage Range Battery Charging Applications," *IEEE Trans. Power Electron.*, Vol. 28, No. 12, pp. 5437-5445, Dec. 2013.
[7] Yihua Hu, Wenping Cao, Stephen J. Finney, Weidong Xiao, et al, "New Modular Structure DC-DC Converter Without Electrolytic Capacitors for Renewable Energy Applications," *IEEE Trans. Sustainable Energy*, Vol. 5, No. 4, pp. 1184-1192, Oct. 2014.
[8] Huiqing Wen, Weidong Xiao, and Bin Su, "Nonactive Power Loss Minimization in a Bidirectional Isolated DC-DC Converter for Distributed Power Systems," *IEEE Trans. Ind. Electron.*, Vol. 61, No. 12, pp. 6822-6831, Dec. 2014.
[9] W. Sun, H. Wu, H. Hu, and Y. Xing, "Resonant Tank Design Considerations and Implementation of a LLC Resonant Converter with a Wide Battery Voltage Range," *Journal of Power Electronics*, Vol. 15, No. 6, pp. 1146-1455, Nov. 2015.
[10] H. Wang, S. Dusmez, and A. Khaligh. "A Novel Approach to Design EV Battery Chargers Using SEPIC PFC Stage and Optimal Operating Point Tracking Technique for LLC Converter," in *Proc. IEEE Appl. Power Electron. Conf. Expo.*, pp. 1683-1689, 2014.
[11] B. K. Lee, J. P. Kim, S. G. Kim, and J. Y. Lee, "A PWM SRT DC_DC Converter for 6.6-kW EV Onboard Charger," *IEEE Trans. Ind. Electron.*, vol. 63, no. 2, pp. 894–902, Feb. 2016.
[12] Haoyu Wang, "A Pulse Width Modulated LLC Type Resonant Topology Adpated to Wide Output Voltage Range," in *Proc. IEEE Appl. Power Electron. Conf. Expo.*, pp. 1280-1285, 2016.
[13] Haiyan Pan, Chao He, Farooq Ajmal, Hengling Chen, Guozhu Chen, "Pulse-width modulation control strategy for high efficiency LLC resonant converter with light load applications," *IET Power Electron.*, Vol. 7, No. 11, pp. 2887-2894, Aug. 2013.
[14] Junichi Yamamoto, Toshiyuki Zaitsu, Seiya Abe, Tamotsu Ninomiya, " PFM and PWM Hybrid controlled LLC converter," *IEEE International Power Electron. Conf.*, pp. 177-182, May 2014.
[15] Q. Chen, J. Wang, Y. Ji, and S. Liang, "Soft starting strategy of bidirectional LLC resonant DC-DC transformer based on phase-shift control," in *Proc. of IEEE Conf. Ind. Electron. and Appl.*, pp. 318-322, 2014.
[16] F. Musavi, M. Craciun, D.S. Gautam, W. Eberle, W.G. Dunford, "Control Strategies for Wide Output Voltage Range LLC Resonant DC-DC Converters in Battery chargers," *IEEE Trans. Power Electron.*, Vol. 63, No. 3, pp. 1117-1125, Mar. 2014.
[17] B. Yang, " Topology investigation for frontend DC/DC power conversion for distributed power systems," Ph. D. dissertation, Virginia Polytechnic Institute and State University, Blacksburg, VA, 2003.
[18] W. Feng and F. C. Lee, "Optimal trajectory control of LLC resonant converters for soft start-up," *IEEE Trans. Power Electron.*, Vol. 29, No. 3, pp. 1461–1468, Mar. 2014.
[19] C. Fei, W. Feng, F. C. Lee, andQ. Li, "State-trajectory control of LLC converter implemented by microcontroller," in *Proc. Appl. Power Electron. Conf. Expo.*, pp. 1045–1052, 2014.
[20] R. Zheng, B. Liu, and S. Duan, "Analysis and parameter optimization of start-up process for LLC resonant converter," *IEEE Trans. Power Electron.*, vol. 30, no. 12, pp. 7113–7122, Dec. 2015.
[21] D. Fu, F. C. Lee, Y. Liu, and M. Xu, "Novel Multi-element resonant converters for front-end DC/DC converters," in *Proc. IEEE Power Electron. Spec. Conf.*, pp. 358–364, 2008.
[22] D. Huang, P. Kong, F. C. Lee, and D. Fu, "A novel integrated multi-elements resonant converter," in *Proc. IEEE Energy Convers. Congr. Expo.*, pp. 3808–3815, 2011.
[23] T. Mishima, H. Mizutani, and M. Nakaoka, "An LLC resonant fullbridge inverter-lin DC-DC converter with an anti-resonant circuit for practical voltage step-up/down regulation," in *Proc. IEEE Energy Convers. Congr. Expo.*, pp. 3533–3540, 2012.
[24] T. Mishima, H. Mizutani, and M. Nakaoka, "A Sensitivity-Improved PFM LLC Resonant Full-Bridge DC-DC Converter with LC Anti-Resonant Tank Circuitry," in *IEEE Trans. Power Electron.*, in press.
[25] H. Wu, X. Jin, H. Hu, and Y. Xing, "Multielement Resonant Converters With a Notch Filter on Secondary Side," *IEEE Trans. Power Electron.*, Vol. 31, No. 6, pp. 3999–4004, Jun. 2016.
[26] R. Ren, F. Zhang, Z. Shen, and S. Liu, "The third harmonics current injection scheme for LLC topology to reduce the RMS of the output current," in *Proc. IEEE Appl. Power Electron. Conf. Expo.*, pp. 1435–1439, 2015.
[27] S. De Simone, C. Adragna, and C. Spini, " Design guideline for magnetic integration in LLC resonant converters," in *Proc. Int. Symp. Power Electron., Electr. Drives, Autom. Motion 2008*, pp. 950–957.
[28] D. Huang, F. C. Lee, and D. Fu, "Classification and Selection Methodology for Multi-Element Resonant Converters," in *Proc. IEEE Appl. Power Electron. Conf. Expo.*, pp. 558–565, 2011.
[29] M. Kim, S. Noh, and S. Choi, "New Symmetrical Bidirectional L3C Resonant DC-DC Converter with Wide Voltage Range," in *Proc. IEEE Appl. Power Electron. Conf. Expo.*, pp. 860–863, 2016.

**Wenjin Sun** was born in Jiangsu Province, China, in 1988. He received his B.S. degree in Electrical Engineering from the Nanjing University of Aeronautics and Astronautics (NUAA), Nanjing, China, in 2011, where he is presently working towards his Ph.D. degree in Electrical Engineering. His current research interests include the topologies and control of power converters, distributed power generation and spacecraft power systems.

**Xiang Jin** was born in Hubei Province, China, in 1991. He received his B.S. and M.S. degrees in Electrical Engineering from Nanjing University of Aeronautics and Astronautics (NUAA), Nanjing, China, in 2013 and 2016, respectively. His current research interests include the topologies and control of power converters, distributed power generation and spacecraft power systems.

**Li Zhang** was born in Jiangsu Province, China, in 1985. He received his B.S. and Ph.D. degrees in Electrical Engineering from the Nanjing University of Aeronautics and Astronautics (NUAA), Nanjing, China, in 2007 and 2012, respectively. He was a Post-Doctoral Research Fellow in the Department of Electrical Engineering, Tsinghua University, Beijing, China, from 2012 to 2014. In 2014, he joined the Faculty of Electrical Engineering, Hohai University, Nanjing, China, where he is presently working as an Associate Professor. His current research interests include the topologies and control of dc-ac converters and distributed generation technology.

**Haibing Hu** received his B.S. degree from the Hunan University of Technology, Hunan, China, in 1995; and his M.S. and Ph.D. degrees in Electrical Engineering from Zhejiang University, Zhejiang, China, in 2003 and 2007, respectively. Since 2007, he has been with the Faculty of Electrical Engineering, Nanjing University of Aeronautics and Astronautics (NUAA), Nanjing, China, where he is presently working as a Professor in the College of Automation Engineering. From 2009 to 2012, he was a Senior Research Fellow in the Department of Electrical Engineering, University of Central Florida, Orlando, FL, USA. He is the author or coauthor of more than 90 technical papers published in journals and conference proceedings. His current research interests include digital control in power electronics, multilevel inverters, digital control system integration for power electronics, and the application of power electronics to distributed energy systems and power quality.

**Yan Xing** was born in Shandong Province, China, in 1964. She received her B.S. and M.S. degrees in Automation and Electrical Engineering from Tsinghua University, Beijing, China, in 1985 and 1988, respectively; and her Ph.D. degree in Electrical Engineering from the Nanjing University of Aeronautics and Astronautics (NUAA), Nanjing, China, in 2000. Since 1988, she has been with the Faculty of Electrical Engineering, NUAA, and is presently working as a Professor in the College of Automation Engineering. She has authored or coauthored more than 100 technical papers published in journals and conference proceedings and has published three books. Her current research interests include the topologies and control of dc-dc and dc-ac converters.